Controlling core-hole lifetime through an x-ray planar cavity

Xin-Chao Huang,[1] Xiang-Jin Kong,[2] Tian-Jun Li,[1] Zi-Ru Ma,[1] Hong-Chang Wang,[3] Gen-Chang Liu,[4] Zhan-Shan Wang,[4] Wen-Bin Li,[4,*] and Lin-Fan Zhu[1,†]

[1]*Hefei National Laboratory for Physical Sciences at Microscale and Department of Modern Physics, University of Science and Technology of China, Hefei, Anhui 230026, People's Republic of China*

[2]*Department of Physics, National University of Defense Technology, Changsha, Hunan 410073, People's Republic of China*

[3]*Diamond Light Source, Harwell Science and Innovation Campus, Didcot, Oxfordshire OX11 0DE, United Kingdom*

[4]*MOE Key Laboratory of Advanced Micro-Structured Materials, Institute of Precision Optical Engineering (IPOE), School of Physics Science and Engineering, Tongji University, Shanghai 200092, People's Republic of China*

(Received 5 May 2020; revised 30 May 2021; accepted 8 July 2021; published 16 July 2021)

It has long been believed that the core-hole lifetime (CHL) of an atom is an intrinsic physical property, and controlling it is significant yet is very hard. Here, the CHL of the $2p$ state of a W atom is manipulated experimentally by adjusting the emission rate of a resonant fluorescence channel with the assistance of an x-ray thin-film planar cavity. The enhanced emission rate is linearly accelerated by the photonic density of states inside the cavity, which can be directly controlled by adjusting the cavity field amplitude through choosing different cavity modes or changing the angle offset in experiment. This experimental observation is in good agreement with the prediction of a developed theoretical model. It is found that the manipulated resonant fluorescence channel can even dominate the CHL. The controllable CHL realized here will facilitate the nonlinear investigations and modern x-ray scattering techniques in the hard x-ray region.

DOI: 10.1103/PhysRevResearch.3.033063

I. INTRODUCTION

The particularity of an inner-shell excitation or ionization is to produce a core vacancy, which has a finite lifetime, i.e., the so-called core-hole lifetime (CHL), and then it decays into lower-lying states. There are two main relaxation pathways, i.e., radiative (fluorescence) and nonradiative (Auger decay or autoionization) channels, and the CHL is determined by the total decay rate of all relaxation channels. Normally, the Auger effect dominates the decay routes of the K shell for low-Z atoms [1] and L and M shells for higher-Z atoms [2], so the CHL is sometimes called the Auger lifetime. The CHL has long been considered an intrinsic factor and controlling it is impossible because the relaxation channels are hard to manipulate with common methods.

Nevertheless, an adjustable CHL is strongly desired, since CHL changes are useful to detect ultrafast dynamics. An adjustable CHL is needed to give deep insight into nonlinear light-matter interaction with the advent of the x-ray free electron laser (XFEL), because the ratio of CHL-to-XFEL pulse width does matter for multiphoton ionization [3], two-photon absorption [4], population inversion [5], and stimulated emission [6,7]. The CHL is also a key factor in the resonant x-ray scattering (RXS) process [8,9], where the dynamics of the core-excited state is controlled by the duration time, which is determined by both energy detuning and the CHL [10]. Because of the lack of an efficient method to manipulate CHL experimentally, the controlling scheme for the duration time has been based on energy detuning up to now [11–16]. The dynamics of the core-excited state determines the application range of RXS techniques, e.g., resonant inelastic x-ray scattering (RIXS) [9]. Since Coulomb interaction between core-hole and valence electrons only occurs during the existence of the core-excited state, the relative time scale between the CHL and elementary excitations governs the effectiveness of indirect RXIS [17–19], especially for charge and magnon excitations [18,20–23]. In time-resolved RIXS, the CHL also needs to be flexibly adjusted to pursue a higher time resolution [24–27]. Therefore, a controllable CHL will be very useful and thus is strongly desired, from both fundamental and application perspectives.

Because the CHL is determined by the total decay rate of all relaxation channels, controlling the CHL means having manipulatable decay channels, at least one of them, which is a challenging task. A stimulated emission channel could be opened by intense and short x-ray pulses to accelerate the CHL [6,7], but such a scheme can only be implemented in XFEL. The present work proposes another scheme to control the spontaneous emission channel. R. Feynman once said that the theory behind chemistry is quantum electrodynamics (QED) [28], indicating that the spontaneous emission rate of an atom depends on the environment (photonic density of states). A cavity is an outstanding system to robustly structure

*wbli@tongji.edu.cn
†lfzhu@ustc.edu.cn

the environment and modify the spontaneous emission rate in the visible wavelength regime [29,30], known as cavity QED. With the dramatic progress in new-generation x-ray sources and thin-film technology, the cavity-QED effect in the hard x-ray range was demonstrated in the laboratory using a thin-film planar cavity with nuclear resonance, e.g., the collective Lamb shift [31], electromagnetically induced transparency [32], spontaneously generated coherences [33], Fano interference [34], group velocity control for x-ray photons [35], and collective strong coupling of x-rays and nuclei [36], as well as with electronic resonance, e.g., spectral control of the L-edge transition [37] and directional fluorescence emission [38], which breeds the new field of x-ray quantum optics [39] and opens up an effective way to control the core-hole lifetime in the x-ray region.

In this work, a controllable CHL for the $2p$ state of the W atom is realized by adjusting the spontaneous emission rate of the resonant fluorescence channel with the assistance of an x-ray planar cavity. WSi_2 has a remarkable white line around the L_{III} edge of W, which is a resonant channel and generally known to be associated with an atomiclike electric dipole allowed transition, from an inner shell, $2p$, to an unoccupied level, $5d$ [40,41]. Inside the cavity, the emission rate of the resonant channel depends on the photonic density of states where the atom is located, which can be modified by the cavity field amplitude in experiments. Because a thin-film planar cavity can only enhance the photonic density of states, and not suppress it, only CHL shortening is realized in the present experiment. As long as the cavity effect is strong enough, the total decay rate will show measurable changes and lead to a controllable CHL. In this work, the enhanced spontaneous emission rate could be even higher than the natural decay rate, indicating that the limitation of unchangeable Auger and radiative decay channels is broken.

II. THEORETICAL MODEL AND EXPERIMENTAL METHOD

Figure 1(a) depicts the cavity structure used in the present work. The thin-film cavity is made of a multilayer of Pt and C. The top and bottom layers of Pt with a high electron density are used as mirrors, and the top one is relatively thin so that the x-ray can couple to the cavity. The layers of C in the middle with a low electron density are used to guide the x-ray and to stack the cavity space. In this design, at certain incident angles $\theta_{\rm th}$ below the critical angle of Pt, the x-ray can resonantly excite specific cavity guided modes where dips in the rocking curve appear as shown in Fig. 1(b). In the present work, $\theta_{\rm th}$ are $\theta_{\rm 1st} = 0.218^\circ$, $\theta_{\rm 3rd} = 0.312^\circ$, and $\theta_{\rm 5th} = 0.440^\circ$ for the first, third, and fifth odd orders of the cavity mode. Then the coupling between the cavity and the atom is built by embedding a thin layer of WSi_2 in the middle of the cavity where the cavity field amplitudes are the strongest. The field distributions of the first, third, and fifth orders of the cavity mode are sketched in Fig. 1(a).

As shown in the middle inset in Fig. 1(a), the inner-shell energy-level system is different from the simple two-level one, and both resonant channels and additional processes like inelastic radiative channels (Auger decay channels are not exhibited here) can annihilate the core vacancy state, e.g.,

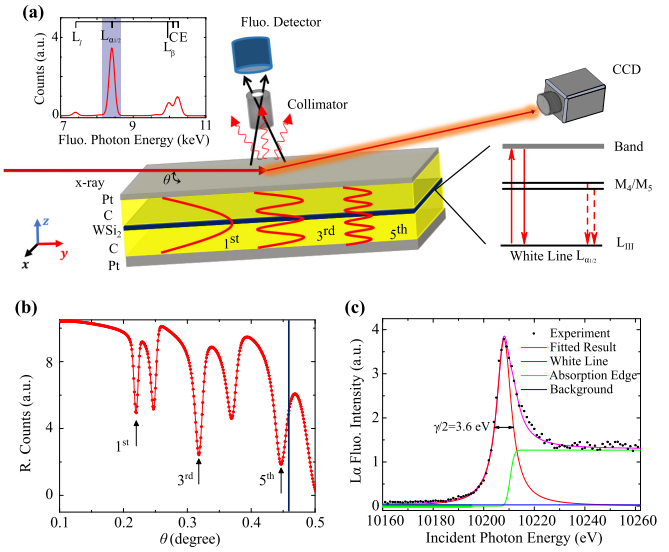

FIG. 1. Schematic for controlling the core-hole lifetime. (a) Cavity sample and measurement setup. The cavity has the structure of Pt (2.1 nm)/C (18.4 nm)/WSi_2 (2.8 nm)/C (18.0 nm)/Pt (16.0 nm)/Si_{100}, and the middle-right inset shows the energy level of the L_{III} edge of the W atom. The sample is probed by a monochromatic x-ray, the resonant fluorescence is measured in the reflection direction by a CCD, and the inelastic fluorescence signals are collected by an energy-resolved fluorescence detector. The distance between collimator and sample surface is 31.0 mm, and the hole diameter and the length of the collimator are 2.8 and 20.1 mm, respectively. An example of the full-range fluorescence spectrum is shown in the inset at the top left, and the gray region corresponds to the fluorescence photon energy of the L_α line. (b) The $\theta - 2\theta$ rocking curve with an incident energy detuning 30 eV from E_0; the vertical blue line indicates the critical angle of Pt (0.46°). (c) The experimental and fitted inelastic fluorescence spectra as a function of the incident photon energy at an incident angle of 3°. Black dots represent experimental results, and solid pink, red, green, and blue lines show the fitted result, Lorentzian resonance line, electronic continuum line, and flat background respectively.

characteristic radiations occur for the radiative channels. An example of the full-range fluorescence spectrum is shown in the top-left inset in Fig. 1(a), where the L_l, L_α, and $L_{\beta 2}$ lines are observed. So the decay width is determined by the total decay rates of all relaxation channels. In experiments, the total decay rate, i.e., the inverse CHL, could be determined by the linewidth of the white line as in Fig. 1(c). Figure 1(c) shows the L_α inelastic fluorescence spectrum as a function of the incident photon energy, which is measured at the large incident angle of 3°. This angle is much larger than the critical angle of Pt, thus the incident x-ray penetrates through the cavity completely, which is like the free space. Therefore, the values of the natural decay width γ and the transition energy E_0 of the white line can be obtained through fitting [Fig. 1(c)]. The custom fit function combines a simple Lorentzian function and a Heaviside step function, which are used to describe the white line and the absorption edge, respectively (see Appendix D).

Excited by the x-ray field, the atom emits the resonant fluorescence through the resonant channel. Here the resonant

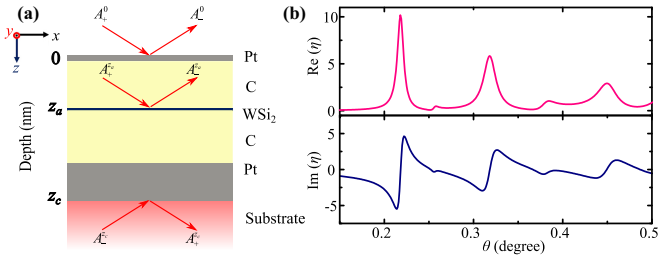

FIG. 2. Schematic of the theoretical model. (a) Sample geometry in the xz plane and schematic of the transfer matrix formulism. (b) Values of $\mathrm{Re}(\eta)$ and $\mathrm{Im}(\eta)$ as a function of the incident angle, which is calculated by a transfer matrix formulism.

behavior of the W atom is reduced to a typical Lorentzian response, and the scattering amplitude of the resonant fluorescence can be written as

$$f = -f_0 \frac{i\gamma_{\mathrm{re}}/2}{\delta + i(\gamma_{\mathrm{re}}/2 + \gamma_{\mathrm{in}}/2)}. \tag{1}$$

The electronic continuum in the higher energy range is not considered here. f_0 is a constant to characterize the resonant fluorescence strength, and δ is the energy detuning between the incident x-ray energy E and the white line transition energy E_0. γ_{re} is the natural spontaneous emission rate of the resonant channel, while γ_{in} is the additional decay rate which sums two branches: the radiative decay rate of the inelastic fluorescence channels γ_{ie} and the nonradiative decay rate of the Auger process γ_{A}, i.e., $\gamma_{\mathrm{in}} = \gamma_{\mathrm{ie}} + \gamma_{\mathrm{A}}$. It is clear that the natural inverse core-hole lifetime is expressed by the sum of all decay rates as $\gamma = \gamma_{\mathrm{re}} + \gamma_{\mathrm{in}}$. Generally, the strongest decay channel is the Auger relaxation for the $\mathrm{L_{III}}$ edge of the W atom in free space, and γ_{ie} and γ_{A} are difficult to adjust, so the CHL has long been considered an intrinsic factor and controlling it is impossible. In the present work, the spontaneous emission rate of the resonant channel is enhanced by introducing the cavity effect, and we show that the cavity effect is strong enough to break the limitation of unchangeable Auger and radiative decay channels.

The x-ray thin-film planar cavity has been demonstrated to have the ability to strengthen the photonic density of states. Recently, spectral control of the L-edge transition [37] and the directional fluorescence emission [38] has been achieved by employing the x-ray thin-film planar cavity, indicating that the x-ray thin-film planar cavity is an effective platform to control the core-hole lifetime for electronic resonance systems. In the linear regime, the photonic density of states is related to the Green function of the multilayer system [29], and Röhlsberger *et al.* connected the Green function with the cavity field amplitude [42], which can be calculated by Parratt's formulism or the transfer matrix method. In the present theory, we employ a transfer matrix method and perform a perturbation expansion of the ultrathin atomic layer [31] to give an analytical expression for the resonant fluorescence. As shown in Fig. 2(a), the field amplitude A^z at position z is connected with A^0 at the surface through a matrix M^z:

$$\begin{pmatrix} A^z_+ \\ A^z_- \end{pmatrix} = M^z \begin{pmatrix} A^0_+ \\ A^0_- \end{pmatrix} = \begin{pmatrix} M^z_{11} M^z_{12} \\ M^z_{21} M^z_{22} \end{pmatrix} \begin{pmatrix} A^0_+ \\ A^0_- \end{pmatrix}. \tag{2}$$

After expanding the matrix of the ultrathin atomic layer (see Appendix A), the enhanced resonant fluorescence in the reflection direction is given in analytical form,

$$r_a = -\frac{id f_0 \times |a^{z_a}|^2 \gamma_{\mathrm{re}}/2}{\delta + \delta_c + i(\gamma_c + \gamma)/2}, \tag{3}$$

where d is the thickness of the atomic layer, and $|a^{z_a}|^2$ is the field intensity where the atom is located. It can be seen that Eq. (3) still has a Lorentzian resonant response, while it contains additional cavity effects: the cavity enhanced emission rate γ_c and the cavity induced energy shift δ_c,

$$\begin{aligned} \gamma_c &= d f_0 \gamma_{\mathrm{re}} \times \mathrm{Re}\,(\eta), \\ \delta_c &= d f_0 \gamma_{\mathrm{re}} \times \mathrm{Im}\,(\eta), \\ \eta &= p(z_a) q(z_a). \end{aligned} \tag{4}$$

Thus the emission rate is enhanced by a factor of $\mathrm{Re}(\eta)$, where $p(z_a) = M^{z_a}_{11} + M^{z_a}_{21}$ and $q(z_a) = M^{z_a}_{12} + M^{z_a}_{22}$ are the field amplitudes corresponding to the wave scattered from the up (down) direction into both the up and the down directions at the position of the atomic layer (Appendix A). Note here that the photonic density of states is directly related to the cavity field amplitudes [42], so Eq. (4) conforms to the typical cavity effect [30], which describes the well-known linear relation between lifetime shortening and photonic density of states strengthening. It is clear that the real part of η is an essential factor to control the enhanced emission rate, and the energy shift is modified by the imaginary part of η. The real and imaginary parts of η as a function of the incident angle calculated by the present transfer matrix formulism are depicted in Fig. 2(b). Figure 2(b) indicates that γ_c and δ_c are simultaneously modified by the incident angle around the mode angles of the odd orders, which has been observed by Haber *et al.* recently [37]. On the other hand, Fig. 2(b) suggests that the strongest enhanced emission rate can be achieved without introducing additional energy shift by exactly choosing the angles of odd order of the cavity mode, which will be more convenient for studying the individual influence of the CHL on core-hole dynamics (see Appendix E).

The fully controllable resonant channel makes an adjustable total inverse core-hole lifetime,

$$\Gamma_n = \gamma_c + \gamma_{\mathrm{re}} + \gamma_{\mathrm{ie}} + \gamma_{\mathrm{A}}, \tag{5}$$

where all four contributions are included. Herein γ_c is the cavity enhanced emission rate, and $\gamma = \gamma_{\mathrm{re}} + \gamma_{\mathrm{ie}} + \gamma_{\mathrm{A}}$ is the natural inverse CHL as the sum of three branches: the natural spontaneous emission rate of the resonant fluorescence channel, the radiative decay rate of the inelastic fluorescence channels, and the Auger decay rate. γ is a fixed value which is obtained from Fig. 1(c), i.e., $\gamma/2 = 3.6$ eV. As long as γ_c is large enough, this controllable part will dominate the CHL.

The simplified energy levels including the cavity effect are shown in Fig. 3 (Auger decay channels are not exhibited here). The enhanced spontaneous emission rate for the resonant fluorescence channel is labeled $(1 + \mathrm{Re}(\eta))\gamma_{\mathrm{re}} = \gamma_{\mathrm{re}} + \gamma_c$. As discussed above, the total inverse core-hole lifetime determines the linewidth of the inelastic fluorescence, i.e., the inelastic scattering spectrum. We employ an RXS formalism known as the Kramers-Heisenberg equation to characterize

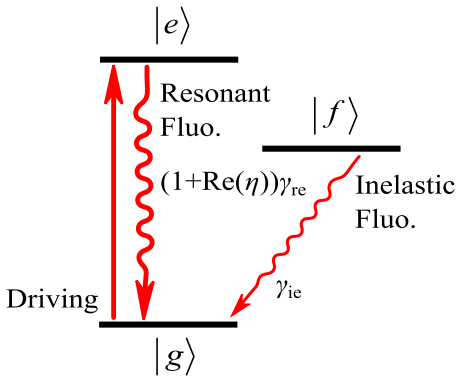

FIG. 3. The simplified energy levels. The driving is shown by the red arrow, and the enhanced spontaneous emission is represented by the thick wavy red arrow. The inelastic fluorescence decay is shown by the thin wavy diagonal red arrow.

the inelastic scattering [8,9] as

$$F_{\rm if}(\vec{k},\vec{k}',\omega,\omega') = \frac{\langle f|\hat{D}'|n\rangle\langle n|\hat{D}|i\rangle}{\delta + i\Gamma_n/2}. \tag{6}$$

Herein the initial state $|i\rangle = |g,\vec{k}\rangle$, the final state $|f\rangle = |f,\vec{k}'\rangle$, and the intermediate state $|n\rangle = |e,0\rangle$. $\vec{k}$ is the wave vector and $\hat{D}$ is the transition operator. For the present work, an intermediate state and a final state are considered since we choose the white line of the L_{III} edge and L_α lines ($L_{\alpha1}$ is much larger than $L_{\alpha2}$) with energy E' are selected to plot the inelastic fluorescence spectrum. Equation (6) indicates that CHL changes can be monitored by the inelastic fluorescence spectrum. Moreover, the values of the cavity enhanced emission rate can be obtained by Eq. (5) as $\gamma_c = \Gamma_n - \gamma$, which is used to quantitatively discuss the cavity effect.

The multilayer was deposited onto a polished silicon wafer (100) using the DC magnetron sputtering method, which is popular for fabricating diverse cavity structures [31–38]. The deposition rate was calibrated carefully. Before deposition, the chamber was evacuated to reach the base pressure of 2×10^{-4} Pa. Argon with a purity of 99.999% was used as the sputtering gas and the working pressure was kept at 1.0 mTorr during the deposition. The powers and voltages applied on Pt, C, and WSi_2 were set at 20 W/360 V, 100 W/420 V, and 25 W/340 V, respectively. The individual layer thickness was controlled by the relevant deposition time to guarantee the layer thickness with an accuracy of better than 1 Å.

The measurement was performed on the B16 Test beamline in the Diamond Light Source. A monochromatic x-ray from a double-crystal monochromator was used to scan the incident x-ray energy, and two far apart slits were used to obtain a good collimation beam with the small vertical beam size of about 50 μm. As shown in Fig. 1(b), in experiments the $\theta - 2\theta$ rocking curve with an incident energy detuning 30 eV from the white line position was measured first to find the desired specific incident angles corresponding to the first, third, and fifth orders of the cavity modes, i.e., the corresponding reflection dips. For a given incident angle, the incident energy E was scanned from 10 161 to 10 261 eV across the transition energy $E_0 = 10\,208$ eV. Then the reflectivity corresponding to the resonant fluorescence was measured by a CCD detector in the reflection direction, and the inelastic fluorescence lines were measured simultaneously by a silicon drift detector (Vortex) with a resolution of about 180 eV in the perpendicular direction. An example of the full-range fluorescence spectrum is shown in the top-left inset in Fig. 1(a), where the energy positions of the L_l, L_α, $L_{\beta2}$, Compton scattering C, and elastic scattering E lines are depicted. The strongest L_α lines ($L_{\alpha1}$ at 8398 eV and $L_{\alpha2}$ at 8335 eV) of W are far from the C, E, and other weak fluorescence lines (9951 eV of $L_{\beta2}$, 7387 eV of L_l, and other negligible lines), so L_α can be extracted separately to plot the inelastic fluorescence spectra. In front of the fluorescence detector, a collimator guarantees a constant detected area of the sample, and the footprint $bw/\sin\theta$ on the sample surface is determined by the beam width bw and the incident angle θ, so the inelastic fluorescence intensities are normalized by taking into account the geometry factor [43]. The size of the sample is 30×30 mm^2, which is larger than the footprint to avoid the beam overpassing the sample length.

III. RESULTS AND DISCUSSION

Figure 4 depicts the results at the exact first, third, and fifth orders to control the CHL without introducing additional energy shift. Figure 4(a) shows the experimental reflectivity curves (filled dots) from two pathways (see Appendix A): the first one of r_0 is from the multilayer cavity itself, where the photon does not interact with the atom, and the second one of r_a is from the resonant atom inside the cavity, i.e., Eq. (3), the enhanced resonant fluorescence. The energy linewidth of the cavity is much larger than that of the atom, which means that r_0 is more like a broad continuum state and r_a is more like a sharp discrete state [34,37,44]. Therefore, the reflectivity curve is a result of Fano interference (see Appendixes A and B). It is shown in Fig. 4(a) that the profiles of the reflectivity curves show a Fano lineshape. The experimental reflectivity curves are fitted by the present theoretical formula $|r_a + r_0|^2$ (see Appendix C) as shown by the solid lines in Fig. 4(a). The present theoretical model for resonant fluorescence does not take into account the influence of the absorption edge due to its electronic continuum nature, and the continuum overlaps the right side of the white line. The sudden increase in the absorption coefficient changes the refractive index and dramatically alters the cavity properties [37]. So the data below 10 220 eV are selected for fitting (labeled by the green region) and good agreements are shown in Fig. 4(a). Above 10 220 eV, it can be easily understood that the theoretical results diverge from the experimental data. The fitted reflectivity curves give the values of $(\gamma_c + \gamma)/2$ as 7.9, 6.9, and 5.2 eV for the first, third, and fifth orders of the cavity mode.

Figure 4(b) shows the experimental and fitted inelastic fluorescence spectra of L_α as a function of the incident x-ray energy for the first, third, and fifth orders. The inelastic fluorescence spectrum is fitted by a custom function combining a simple Lorentz function $L(E)$ with a Heaviside step function $H(E)$ (see Appendix D); herein $L(E)$ with a linewidth Γ_n is used to describe Eq. (6) and $H(E)$ is used to describe the absorption edge. The fitted values of $\Gamma_n/2$ are 8.6, 6.2, and 5.1 eV, which match well the derived values from the

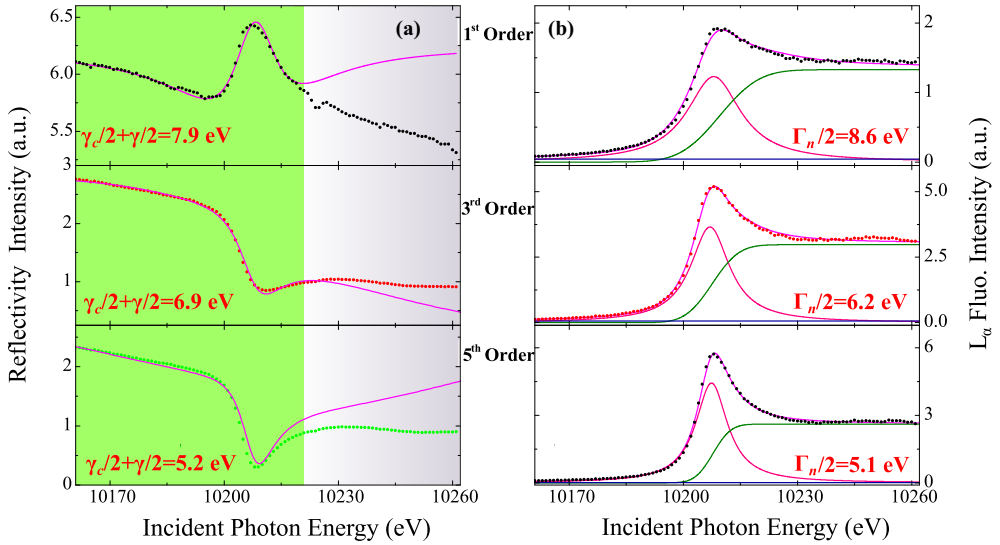

FIG. 4. Resonant fluorescence and inelastic fluorescence spectra. (a) The measured and theoretical reflectivity spectra for the first, third, and fifth orders as a function of the incident photon energy. The pink solid line shows the theoretically fitted result. (b) The measured and fitted inelastic fluorescence spectra of L_α as a function of the incident photon energy. The pink, red, green, and blue solid lines represent the fitted result, Lorentzian resonance line, electronic continuum line, and flat background, respectively.

resonant fluorescence spectra in Fig. 4(a), demonstrating that the shortening of the CHL indeed comes from the regulation of the resonant fluorescence channel. Moreover, the value of $\gamma_c = \Gamma_n - \gamma$ is even larger than γ at first order, indicating that the adjustable resonant channel breaks the limitation of unchangeable Auger and radiative decay channels and dominantly determines the CHL.

The measured inelastic fluorescence 2D spectra are shown in Fig. 5 for selected incident angles around the mode angles of the first, third, and fifth orders ($\theta_{1st} = 0.218°$, $\theta_{3rd} = 0.312°$, and $\theta_{5th} = 0.440°$, respectively). As discussed in Eq. (4), the CHL and the cavity induced energy shift are simultaneously controlled by the incident angle. When the incident angle scans across the mode angle, a phenomenon of the inverse CHL's first increasing to a maximum at the mode angle, then decreasing is observed, along with an additional energy shift, which is demonstrated in Fig. 5. For the third order, the maximum linewidth does not seem to be where the angle offset is 0; this may be due to the occasional angle shift from the instabilities of the goniometer or sample holder. Note here that Fig. 5 suggests a way to continuously modify the CHL but introduce an additional energy shift.

As predicted in Eq. (4), the enhanced emission rate γ_c is linearly connected with the real part of the cavity field amplitude η, and this is essential to discuss the magnitude of the inverse CHL. It should be noted here that the present method to control the CHL is different from the scenario of stimulated emission [6,7], where a nonlinear relationship between the stimulated emission rate and the x-ray field intensity is expected. The present scheme actually employs a cavity to manipulate the enhanced spontaneous emission, whose decay rate is linearly determined by the photonic density of states. All inelastic fluorescence spectra in Fig. 5 are fitted to get the values of Γ_n, and some selected spectra are shown in Fig. 6(a). Then the values of γ_c are obtained based on Eq. (5), and the values of Re(η) are calculated by the transfer matrix formulism as discussed in Fig. 2(b). A good linear relationship between γ_c and Re(η) is depicted in Fig. 6(b), which is consistent with the prediction of Eq. (4).

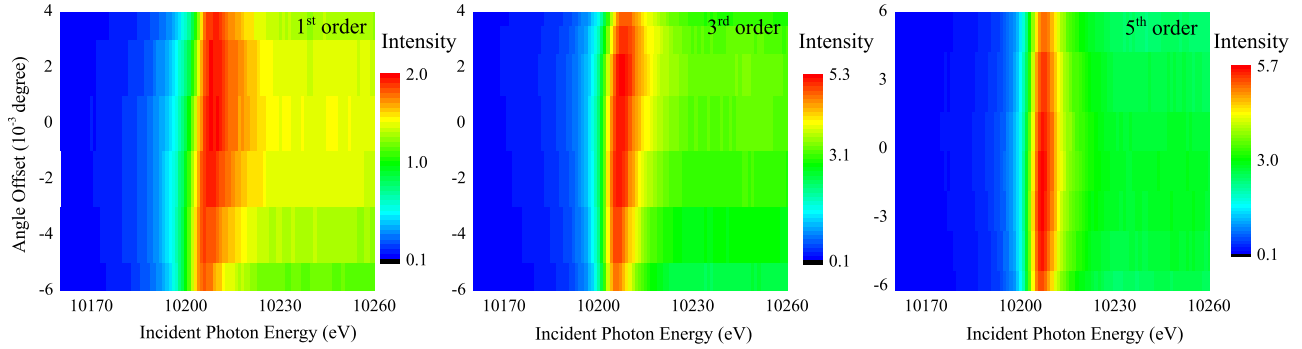

FIG. 5. The 2D inelastic fluorescence spectra as functions of the incident photon energy and angle offset. The angle offset is the deviation between the incident angle and the θ_{1st} (left), θ_{3rd} (middle), and θ_{5th} (right).

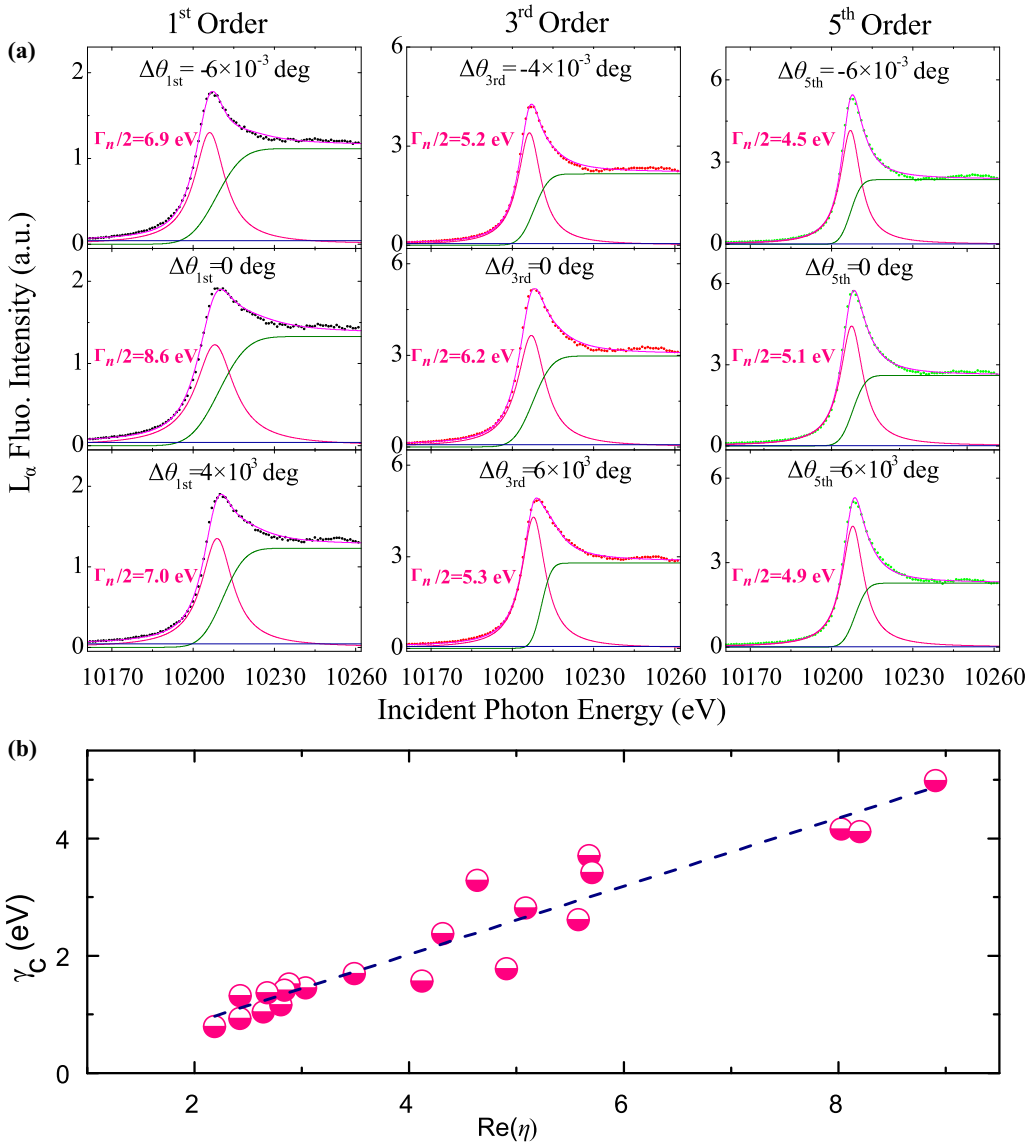

FIG. 6. The linear relationship between the cavity enhanced emission rate and the field amplitude. (a) The measured and fitted inelastic fluorescence spectra for selected angle offsets; the fitted values of $\Gamma_n/2$ for each panel are labeled. (b) Cavity enhanced emission rate γ_c as a function of Re(η). The values of γ_c are derived from the fitted linewidth Γ_n as $\gamma_c = \Gamma_n - \gamma$, and the values of Re($\eta$) are obtained by transfer matrix calculation. The dashed blue line is a linear fitting of the experimental dots to guide the eyes.

Notably, the linear relationship of Eq. (4) between the cavity enhanced emission rate and the field amplitude is the typical cavity Purcell effect [30]. According to Fermi's golden rule, the emission rate of the resonant fluorescence channel is given as

$$\Gamma_{\rm re} = \frac{2\pi}{\hbar^2}\rho(z, E_0)|\langle g|H|e\rangle|^2, \tag{7}$$

where $\rho(z, E_0)$ is the photonic density of states at position z where the atom is located. $|\langle g|H|e\rangle|$ is the transition matrix and H is the atom-field interaction Hamiltonian. It is clear that the emission rate is linearly proportional to the photonic density of states. The multilayer medium affects the photonic density of states, which can be calculated by the complete Green function [29]:

$$\rho(z, E_0) = -\frac{1}{\pi}{\rm Im}[G_0(z, z, E_0) + G_{\rm 1D}(z, z, E_0)]. \tag{8}$$

Herein $G_0(z, z, E_0)$ is the Green function from the vacuum field which contributes to the spontaneous emission rate $\gamma_{\rm re}$, while $G_{\rm 1D}(z, z, E_0)$ is the Green function from the 1D planar cavity which contributes to the cavity enhanced emission rate $\gamma_{\rm c}$. The transfer matrix or Parratt's formalisms give the connection between $G_{\rm 1D}(z, z, E_0)$ and the field amplitude as

$$G_{\rm 1D}(z_i, z_j, E_0) = \frac{i}{2k_z}[p(z_i)q(z_j)\Theta(z_i - z_j) + p(z_j)q(z_i)\Theta(z_j - z_i)], \tag{9}$$

where k_z is the z component of the wave vector, and Θ is the step function. In the present work, an ultrathin atomic layer located at a position z_a is utilized, so the Green function is reduced to the simple form of

$$G_{\rm 1D}(z_a, z_a, E_0) = \frac{i}{2k_z}\cdot p(z_a)q(z_a), \tag{10}$$

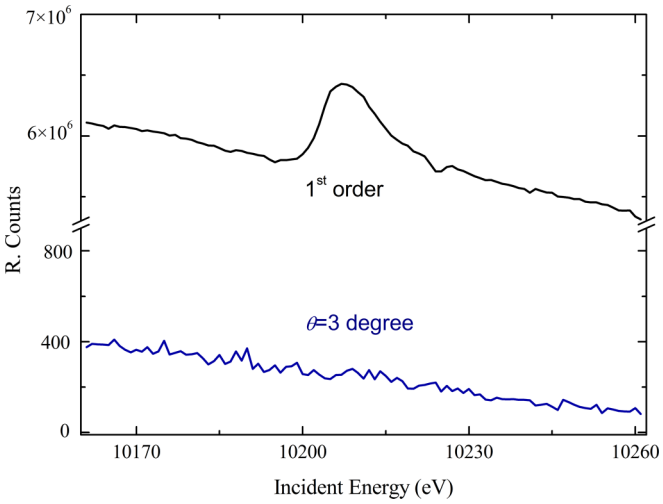

FIG. 7. The experimental reflectivity curve at the first order of the cavity mode and that of the incident angle at 3°. The resonant fluorescence is only detected in the mode angle, and the reflectivity curve at the incident angle of 3° only shows a flat background, without a response of resonant fluorescence.

where $p(z_a) = M_{11}^{z_a} + M_{21}^{z_a}$ and $q(z_a) = M_{12}^{z_a} + M_{22}^{z_a}$ are the field amplitudes corresponding to the wave scattered from the up (down) direction into both the up and the down directions at the position of the atomic layer, which have been discussed with regard to Eq. (4). Inserting Eq. (9) into Eq. (8), the linear relationship between the photonic density of states and the real part of $p(z_a)q(z_a)$, i.e., η, is obtained. Therefore, Eq. (4) is actually identical to the well-known Fermi's golden rule of Eq. (7), and both Eq. (4) and Eq. (7) conform to the typical cavity effect [30], which describes the well-known linear relation between the emission rate enhancement and the strengthening of the photonic density of states. As shown in Fig. 6(b), a good linear relationship between γ_c and Re(η) is depicted, and the intercept of the dashed blue fitted line is as small as −0.3 eV. The tiny nonzero intercept should be due to the accuracies of the experimental results.

When core-hole lifetime shortening takes place the resonant fluorescence has to increase remarkably in the reflection direction, i.e., the resonant fluorescence emits at the angle of the cavity mode; this is a typical directional emission [30] effect. In the x-ray regime, this kind of cavity effect has been proven in nuclear [31–36] and electronic [37,38] resonance systems. To further demonstrate the role of the cavity, the reflectivity curve at the incident angle of 3° is also measured and shown in Fig. 7. For comparison, the reflectivity curve of the first order of the cavity mode is also depicted in the figure. The incident angle of 3° is much larger than the critical angle of Pt (0.46°), thus the incident x-ray almost penetrates through the cavity, which is like the free space. This means that the cavity effect is invalid at a large incident angle and the amplitude of the resonant fluorescence will not be enhanced anymore. It is clear that the reflectivity curve at the incident angle of 3° only shows a flat background, without an obvious response of the resonant fluorescence. The cavity effect is effective only when the incident angle is at the mode angle, where the resonant fluorescence amplitude is enhanced,

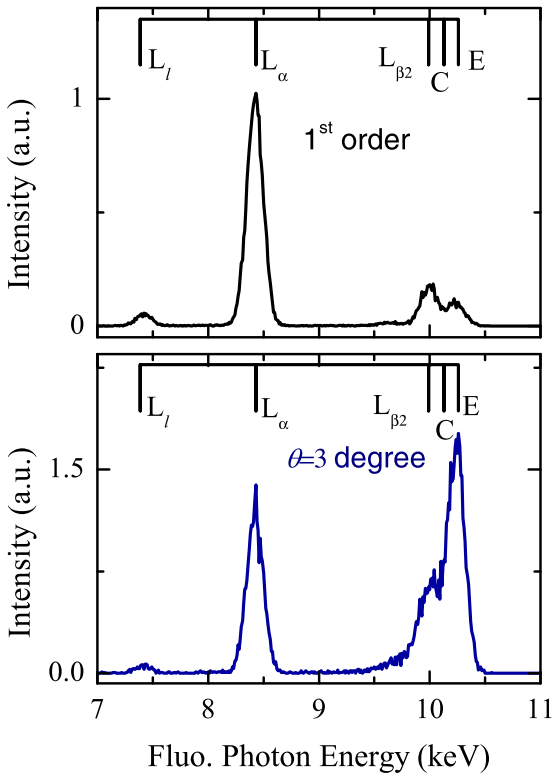

FIG. 8. The full-range fluorescence spectra at an incident angle of the first-order mode and 3°, respectively. The spectra are measured in the perpendicular direction, and the incident photon energy is E_0. The normalization factor from the grazing measurement geometry is taken into account. The energy positions of the L_l, L_α, $L_{\beta 2}$, Compton scattering C, and elastic scattering lines E are depicted.

causing Fano interference along with the reflection coefficient from the multilayer, resulting in peak or window profiles as shown in Figs. 7 and 4(a).

As sketched in Fig. 3, the resonant fluorescence is an elastic process with the excited electron initially promoted from the $2p$ to the $5d$ state. The photon energy of the resonant fluorescence is the same as the incident energy. This means that the resonant fluorescence and the elastic Rayleigh scattering cannot be distinguished either by the reflection or by the fluorescence detectors. However, when the resonant fluorescence increases remarkably in the reflection direction, the intensity of the resonant fluorescence should drop remarkably in other solid angles. Figure 8 shows the full-range fluorescence spectra at incident angles of the first-order mode and 3°, and the incident photon energy is fixed at E_0 in both Figs. 8(a) and 8(b). In the general case, the elastic scattering line (including the resonant fluorescence and the Rayleigh scattering) is stronger than the inelastic fluorescence lines, e.g., the elastic line is stronger than the Lα line as shown in Fig. 8(b). In the spectrum in Fig. 8(a), the intensity of the elastic scattering line decreases and is weaker than the Lα line. Note here that the Rayleigh scattering is from all layers' material of the sample, including Pt, C, WSi_2, and substrate Si; this means that the Rayleigh scattering is a baseline. Therefore, a decrease in intensity of the elastic line indicates that the intensity of the resonant fluorescence drops in the perpendicular direction.

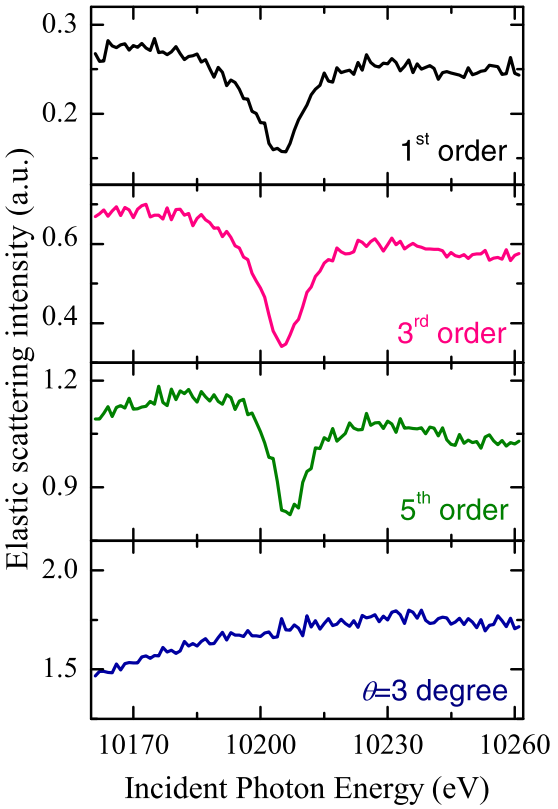

FIG. 9. The elastic scattering spectra as a function of the incident photon energy. The spectra are measured in the perpendicular direction. For comparison the spectra of the incident angle at mode angles of the first order (black line), third order (red line), fifth order (green line), and 3° (blue line) are shown. The elastic scattering is a summation of the resonant fluorescence and the Rayleigh scattering. The Rayleigh scattering is from all materials of the sample, so it is a baseline as shown in the bottom spectrum at the incident angle of 3°. As in Fig. 8, a drop in the intensity of other solid angles means that the resonant fluorescence prefers to emit in the reflection direction.

Figure 9 shows the elastic scattering spectra as a function of the incident photon energy; for comparison the spectra at the incident angles of the first, third, and fifth orders and 3° are given. Figure 9 is obtained by extracting the elastic line separately from the full-range fluorescence spectra. A behavior of intensity dropping is observed when the incident angles are set at mode angles of the first, third, and fifth orders, while the elastic scattering spectrum at the incident angle of 3° is flat. On the other hand, the baselines of the spectra at the incident angles of the first, third, and fifth orders are smaller than that of 3°; this should be because the incident x-ray couples to the cavity, thus the Rayleigh scattering is weaker when the cavity modes are excited.

IV. CONCLUSION

In summary, the present work experimentally demonstrates two control methods to manipulate the core-hole lifetime by constructing an x-ray thin-film planar cavity system: choosing different cavity modes and changing the angle offset. The first one adjusts the core-hole lifetime without introducing an additional energy shift, while the second one can continuously modify the core-hole lifetime but introduce an additional energy shift. The linear relationship between the cavity enhanced emission rate and the photonic density of states, i.e., the field amplitude, is observed in experiments and interpreted by the present theoretical model. Note here that the present method to control the CHL is different from the scenario of stimulated emission [6,7], where a nonlinear relationship is expected between the stimulated emission rate and the x-ray field intensity. The core-hole lifetime changes would be useful to detect ultrafast dynamics. In the RXS process, the duration of the core excited state is determined by both the energy shift and the core-hole lifetime. Utilizing the present cavity technique, the duration of the RXS process can be controlled not only by the energy detuning, but also by the core-hole lifetime (see Appendix E), which will enrich physical studies on RXS. Combined with a high-resolution, ∼100-meV analyzer [45], cavity-manipulating RXS effects such as Raman-Stokes shifts [46], linewidth narrowing [47], and Stokes doubling [48] are expected to be achievable. On the other hand, the cavity structure is suitable for a wide range of x-ray energies, from a few to tens of keV, so the present scheme could be extended to a lot of elements which have a resonant fluorescence channel.

The phenomenon that the core-hole lifetime changes can be monitored by the inelastic fluorescence is also interesting. From the general viewpoint of cavity QED in the optical regime, the inelastic channel is an incoherent process which accelerates the decoherence, so it is regarded as a defect in the system [49]. However, the inelastic channel is a natural character and widely exists in both atomic inner-shell and nuclear resonance systems, e.g., Auger and inelastic fluorescence relaxation pathways for atomic inner-shell transition and internal conversion channels for nuclear transition. Herein we demonstrate that the inelastic fluorescence channels could be very useful to monitor CHL changes and enrich the picture of the cavity effect. The more complex energy levels in the x-ray regime will bring richer physics, e.g., the effect of exchange interaction [50] on inelastic fluorescence channels can be studied.

ACKNOWLEDGMENTS

We thank X.-J. Liu for fruitful discussion about the duration of the core-excited state. This work was supported by the National Natural Science Foundation of China (Grant No. U1932207) and the National Key Research and Development Program of China (Grant Nos. 2017YFA0303500 and 2017YFA0402300). The experiment was carried out in the B16 beamline of the Diamond Light Source Ltd. (No. MM21446-1), United Kingdom. The sample was prepared and precharacterized in the MOE Key Laboratory of Advanced Micro-Structured Materials, Institute of Precision Optical Engineering (IPOE), School of Physics Science and Engineering, Tongji University.

APPENDIX A: THEORY DERIVATION

Here we derive the relationship between the inverse core-hole lifetime and the cavity field amplitude at the position of the atom which is presented in Eq. (4). As discussed in

Fig. 1, the incident x-ray resonantly excites the cavity modes at certain incident angles in the mrad range, which can be identified by the reflection dips in the rocking curve. The field amplitude can be adjusted by choosing different orders of the cavity mode (different dips) or detuning the angle offset from the dips, so the method of manipulating the CHL is convenient. Here we employ a transfer matrix method and perform a perturbation expansion of the ultrathin atomic layer [31] to give the analytical expression for the resonant fluorescence. The resonant behavior of the W atom is reduced to a typical Lorentz response, thus the electronic continuum is neglected, and the atomic layer is thin enough to be free from the self-absorption effect [51].

Following the convention of the transfer matrix formalism, $\vec{A}^z = (A^z_+, A^z_-)^T$ are the field amplitudes at position z, where $\vec{A}^z_+$ and $\vec{A}^z_-$ denote the transmitted and reflected parts, respectively. A^z is connected with A^0 through the matrix M^z, where M^z is obtained by multiplying the propagation matrices of different layers from the cavity surface to the depth position z. Moreover, M^z is also used to give the normalized field amplitude at position z:

$$a^z = \frac{A^z_+ + A^z_-}{A^0} = \left(M^z_{11} + M^z_{21}\right) - \left(M^z_{12} + M^z_{22}\right)\frac{M^{z_c}_{21}}{M^{z_c}_{22}}. \quad \text{(A1)}$$

Next we take into account the atomic layer, which is sandwiched at z_a; the amplitude below the atomic layer should be written as

$$\begin{pmatrix} A^z_+ \\ A^z_- \end{pmatrix} = M^{z-z_a} M_{\text{atom}} M^{z_a} \begin{pmatrix} A^0_+ \\ A^0_- \end{pmatrix} = M \begin{pmatrix} A^0_+ \\ A^0_- \end{pmatrix}, \quad \text{(A2)}$$

where M_{atom} is the propagation matrix of the atomic layer,

$$M_{\text{atom}} = \exp(iF \cdot d),$$
$$F = \begin{pmatrix} f & f \\ -f & -f \end{pmatrix}, \quad \text{(A3)}$$

with d the thickness of the atomic layer. F is the atomic resonant fluorescence scattering matrix, and f is the scattering amplitude with the typical Lorentz form as depicted by Eq. (1). Considering the ultrathin atomic layer as a perturbation and applying expansion for M_{atom}, the complete matrix M from the surface to the cavity bottom can be obtained:

$$M \approx M^{z_c - z_a}(1 + id \cdot F) M^{z_a}. \quad \text{(A4)}$$

The reflection coefficient is given through the convention of the transfer matrix formalism,

$$r = \frac{\vec{A}^0_-}{\vec{A}^0_+} = -\frac{M_{21}}{M_{22}}. \quad \text{(A5)}$$

After calculating Eq. (A3) with the matrix operations ($I = M^{-1}M$, $A^0 = A^0_+$), the reflection coefficient can be expressed as

$$r = r_0 + r_a, \quad r_0 = -\frac{M^{z_c}_{21}}{M^{z_c}_{22}},$$
$$r_a = \frac{idf \times |a^{z_a}|^2}{1 - idf \times (p + qr_0)q}. \quad \text{(A6)}$$

It can be seen from Eq. (A5) that the reflection spectrum is a result of two-path interference. The first path of r_0 is from the multilayer itself, where the photon does not interact with the atom, and the second one of r_a is from the resonant atom inside the cavity, i.e., the resonant fluorescence as discussed in Eq. (3). $p(z_a) = M^{z_a}_{11} + M^{z_a}_{21}$ and $q(z_a) = M^{z_a}_{12} + M^{z_a}_{22}$ are the field amplitudes corresponding to the waves scattered from the up (down) direction into both the up and the down directions. Replacing f with the Lorentzian form of Eq. (1), one can remold r_a into Eq. (3), which contains the enhanced emission rate γ_c and the cavity induced energy shift δ_c:

$$\gamma_c = d f_0 \gamma_{\text{re}} \times \text{Re}(\eta),$$
$$\delta_c = d f_0 \gamma_{\text{re}} \times \text{Im}(\eta),$$
$$\eta = (p + qr_0)q. \quad \text{(A7)}$$

Equations (A5) and (A6) are essential for discussing the resonant fluorescence and the magnitude of the enhanced emission rate γ_c, and the inverse core-hole lifetime should be written as $\Gamma_n = \gamma_c + \gamma$, i.e., Eq. (5). Moreover, a linear relationship between γ_c and the real part of the complex field amplitude η is predicted, which is demonstrated by the experimental results shown in Fig. 6(b). When the incident angle varies around the cavity mode angles (the reflection dips), qr_0 is much smaller than p, and one finds that Eq. (A6) will degenerate to Eq. (4).

APPENDIX B: REFLECTIVITY 2D SPECTRA

The cavity mode has the very broad spectral width of approximately a few hundred eV, which is orders of magnitude greater than the atom width, so r_0 serves as a broad continuum state and r_a serves as a narrow discrete state. Therefore as discussed in Fig. 4(a), $|r_a + r_0|^2$ gives the Fano interference. On the other hand, the relative phase between r_0 and r_a is controlled by the angle offset [37], which gives an angle-dependent asymmetric lineshape, so the Fano interference behavior is shown in Fig. 10.

APPENDIX C: REFLECTIVITY CURVE FITTING

To fit the measured reflectivity spectra, we need to take into account the contribution from the cavity itself r_0, where the photon does not interact with the atom. The analytical form of r_0 can be given by a quantum optics model [52,53], which is more convenient for fitting,

$$r_0 = -1 + \frac{2\kappa_R}{\kappa + i\Delta_c}, \quad \text{(C1)}$$

where κ and κ_R are the decay constant and coupling strength for the planar cavity, and both of them determine the strength of r_0. Δ_c is the cavity detuning, which mainly depends on the angle offset from the angle of a specific cavity mode θ_{th},

$$\Delta_c = \left(\frac{\sin\theta_{\text{th}}}{\sin\theta} - 1\right)E_0. \quad \text{(C2)}$$

However, because a typical Q value of the x-ray planar thin-film cavity is about 100 and the energy range we scan in experiments is 100 eV, θ_{th} will have a small shift in this energy range. As depicted in Fig. 11, the reflection dip moves to a smaller angle as the energy increases. Supposing that the

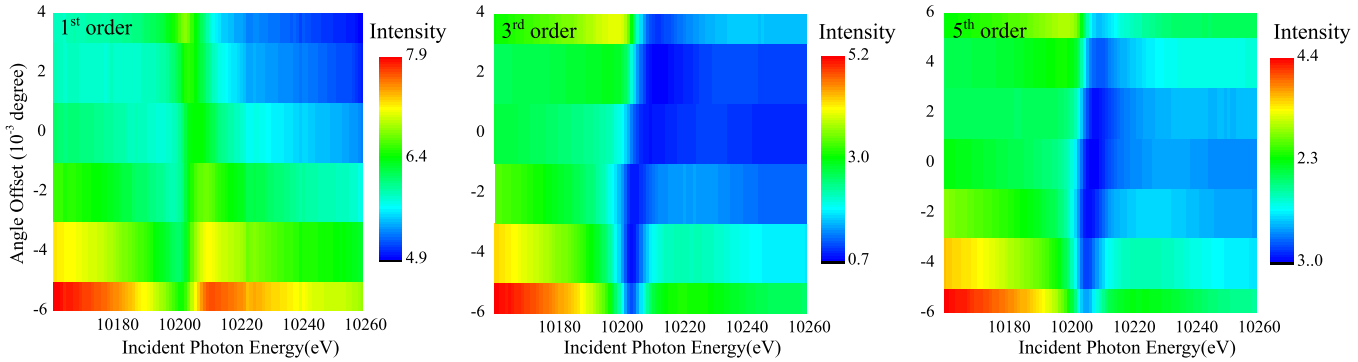

FIG. 10. Two-dimensional maps of the reflectivity spectra vs the energy and angle offset. The angle offset is the deviation between the incident angle and the θ_{1st} (left), θ_{3rd} (middle), and θ_{5th} (right). The figure clearly shows the behavior of Fano interference.

maximum shift is $\Delta\theta_{th}$ and the angle shift has a linear relation with the energy, we rewrite Δ_c as a new form,

$$\theta_{th} \to \theta_{th} - \frac{(E - E_0)}{E_r} \times \Delta\theta_{th}, \tag{C3}$$

where E_r is the energy scanning range and $\Delta\theta_{th}$ is the maximum angular shift in the range of E_r.

Reported by Heeg *et al.* [53], there are two additional effects called heuristic extensions which need to be considered. First, the absorption from the bulk materials of the top Pt layer will weaken the reflectivity intensity. Second, the top Pt layer also makes a tiny dispersion phase. Therefore, r_0 needs to be remolded as

$$r_0 = r_{envelope}(\theta)\left(1 \times e^{i(\pi-\varphi)} + \frac{2\kappa_R}{\kappa + i\Delta_c}\right), \tag{C4}$$

where $r_{envelope}(\theta)$ is used to include the first effect, and a tiny phase shift φ is used to consider the second effect.

Then the experimental reflectivity spectrum can be fitted by the form of intensity,

$$R = c_1|r_0 + c_2 \cdot r_a|^2 + c_3, \tag{C5}$$

where c_1, c_2, and c_3 are constants. c_1 is used to fit the experimental counts, and c_3 is used to consider a constant background. $c_2 < 1$ is used to take into account the absorption effect from the multilayer materials, which weakens the atom resonance. The fitted results for reflectivity spectra of the first, third, and fifth orders are shown in Fig. 4(a).

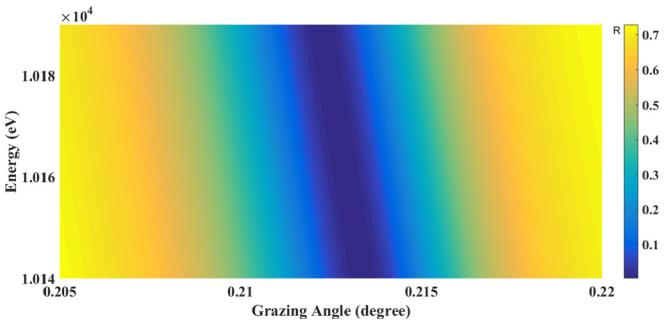

FIG. 11. Empty cavity reflectivity as functions of the photon energy and grazing angle. The 2D spectrum is calculated by Parratt's formulism. The angle of the first order of the cavity mode, i.e., the reflection dip, moves to a smaller angle as the energy increases.

APPENDIX D: INELASTIC FLUORESCENCE SPECTRUM FITTING

The inelastic fluorescence spectra are fitted by a custom function $F(E)$ combining a simple Lorentz function $L(E)$ and a Heaviside step function $H(E)$. $L(E)$ is used to describe the remarkable white line and $H(E)$ is used to describe the absorption edge,

$$F(E) = aL(E) + bH(E) + c, \tag{D1}$$

where a and b are two constants, and c is used to consider a constant background. To describe an edge with a slope, the Heaviside step function is constructed by indefinite integrals of the Gauss function as

$$H(E) = \frac{1}{\sqrt{2\pi}\sigma}\int_{-\infty}^{E} e^{-\frac{(t-E_{ae})^2}{2\sigma^2}} dt, \tag{D2}$$

where σ and E_{ae} characterize the slope and position of the absorption edge, respectively. Then Eq. (D1) is used to fit the inelastic fluorescence spectra as shown in Figs. 4(b) and 6(a).

APPENDIX E: DURATION TIME OF RXS

The radiative RXS amplitude (the nonradiative one has the same form as the radiative one but with $\hat{D}'$ replaced with the Coulomb operator $\hat{Q}$) or so-called inelastic scattering amplitude is written as Eq. (6); it is a projection of the wave packet Ψ on a particular final state $|f\rangle$,

$$F_{if} = -i\langle f|\Psi\rangle,$$
$$\Psi = i\sum_n \frac{\hat{D}'|n\rangle\langle n|\hat{D}|i\rangle}{\delta + i\Gamma_n/2}; \tag{E1}$$

the summation of the intermediate state $|n\rangle$ is included here to be consistent with the general form [9]. The time evolutions of the scattering amplitude and Ψ are given by the Fourier transform of Eq. (E1) based on the theoretical works by Gel'mukhanov and Ågren [8],

$$F_{if}(\tau) = -i\langle f|\Psi_T(\tau)\rangle,$$
$$\Psi_T(\tau) = \int_0^\tau \exp[-t(\Gamma_n/2 - i\delta)]\hat{D}'\psi(t)dt, \tag{E2}$$

where $\psi(t)$ is the wave packet of the intermediate state; when $t = 0$, the intermediate state is excited from the ground state as $\psi(0) = \hat{D}|f\rangle$. The time dependence of $\Psi_T(\tau)$ is decided by the phase factor $\exp[-t(\Gamma_n/2 - i\delta)]$. This phase factor can be rewritten in a new form as $\exp[-t/T]$, and T is a complex time:

$$T = (\Gamma_n/2 - i\delta)^{-1} = T_{\Gamma_n} + iT_\delta,$$
$$T_{\Gamma_n} = \frac{\Gamma_n/2}{(\Gamma_n/2)^2 + \delta^2}, \quad T_\delta = \frac{\delta}{(\Gamma_n/2)^2 + \delta^2}. \tag{E3}$$

One can imagine two situations. The first is that $\Gamma_n/2$ is very large, so the decay rate of $\Psi_T(\tau)$ is quite fast and the long-time contribution to the scattering amplitude is very small. The second one is that δ is very large, and the fast oscillation can also suppress the contribution from the long-time range [the amplitude from different times t_1 and t_2 interfere destructively and quickly due to the phase difference $\delta(t2 - t1)$, resulting in a negligible integrated value], so T_δ is called the dephasing time and the energy detuning can also influence the core-hole dynamics. Therefore, the duration time of the RXS process is determined by both Γ_n and δ:

$$|T| = \frac{1}{\sqrt{(\Gamma_n/2)^2 + \delta^2}}. \tag{E4}$$

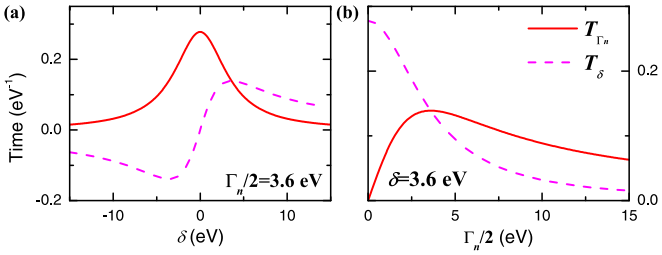

FIG. 12. Dependencies of the real and imaginary parts of the duration time on the energy detuning and the inverse core-hole lifetime.

As shown in Fig. 12, the real T_{Γ_n} and the imaginary T_δ of T depend differently on the energy detuning and the core-hole lifetime. In Fig. 12(a), the duration time can be controlled by the energy detuning, which is successful in interpreting the energy-dependent RXS phenomena and easy to carry out in experiments. But for Fig. 12(b), there has previously been a lack of an efficient method to adjust Γ_n experimentally. So the controlling schemes for duration were almost based on energy detuning previously [11–16]. The present work provides a valid way to control Γ_n experimentally, which would enrich studies on the RXS process. For example, not only the control of energy detuning, but also the control of the core-hole lifetime for extensive effects, such as Raman-Stokes shifts [46], linewidth narrowing [47], and Stokes doubling [48], could be studied in future experiments.

[1] P. Auger, Comptes Rendus **180**, 65 (1925).
[2] M. O. Krause, J. Phys. Chem. Ref. Data **8**, 307 (1979).
[3] H. Fukuzawa, S. K. Son, K. Motomura, S. Mondal, K. Nagaya, S. Wada, X. J. Liu, R. Feifel, T. Tachibana Y. Ito *et al.*, Phys. Rev. Lett. **110**, 173005 (2013).
[4] K. Tamasaku, E. Shigemasa, Y. Inubushi *et al.*, Phys. Rev. Lett. **121**, 083901 (2018).
[5] H. Yoneda, Y. Inubushi, K. Nagamine *et al.*, Nature (London) **524**, 446 (2015).
[6] B. Wu, T. Wang, C. E. Graves *et al.*, Phys. Rev. Lett. **117**, 027401 (2016).
[7] Z. Chen, D. J. Higley, M. Beye, M. Hantschmann, V. Mehta, O. Hellwig, A. Mitra, S. Bonetti, M. Bucher, S. Carron *et al.*, Phys. Rev. Lett. **121**, 137403 (2018).
[8] F. Gel'mukhanov and H. Ågren, Phys. Rep. **312**, 87 (1999).
[9] L. J. P. Ament, M. van Veenendaal, T. P. Devereaux, J. P. Hill, and J. van den Brink, Rev. Mod. Phys. **83**, 705 (2011).
[10] F. Gel'mukhanov, P. Sałek, T. Privalov, and H. Ågren, Phys. Rev. A **59**, 380 (1999).
[11] P. Skytt, P. Glans, J.-H. Guo, K. Gunnelin, C. Såthe, J. Nordgren, F. K. Gel'mukhanov, A. Cesar, and H. Ågren, Phys. Rev. Lett. **77**, 5035 (1996).
[12] R. Feifel, A. Baev, F. Gelmukhanov *et al.*, Phys. Rev. A **69**, 022707 (2004).
[13] V. Kimberg, A. Lindblad, J. Söderström, O. Travnikova, C. Nicolas, Y. P. Sun, F. Gel'mukhanov, N. Kosugi, and C. Miron, Phys. Rev. X **3**, 011017 (2013).
[14] R. Feifel and M. N. Piancastelli, J. Electron Spectrosc. Relat. Phenom. **183**, 10 (2011).
[15] P. Morin and C. Miron, J. Electron Spectrosc. Relat. Phenom. **185**, 259 (2012).
[16] C. Miron and P. Morin, *Handbook of High-Resolution Spectroscopy* (Wiley, Chichester, UK, 2011), pp. 1655–1690.
[17] L. J. P. Ament, F. Forte, and J. van den Brink, Phys. Rev. B **75**, 115118 (2007).
[18] L. J. P. Ament, G. Ghiringhelli, M. M. Sala, L. Braicovich, and J. van den Brink, Phys. Rev. Lett. **103**, 117003 (2009).
[19] M. Dean, R. Springell, C. Monney *et al.*, Nat. Mater. **11**, 850 (2012).
[20] J. van den Brink, Eur. Phys. Lett. **80**, 47003 (2007).
[21] M. W. Haverkort, Phys. Rev. Lett. **105**, 167404 (2010).
[22] C. Jia, K. Wohlfeld, Y. Wang, B. Moritz, and T. P. Devereaux, Phys. Rev. X **6**, 021020 (2016).
[23] T. Tohyama and K. Tsutsui, Int. J. Mod. Phys. B **32**, 1840017 (2018).
[24] M. P. Dean, Y. Cao, X. Liu *et al.*, Nat. Mater. **15**, 601 (2016).
[25] Y. Wang, M. Claassen, C. D. Pemmaraju, C. Jia, B. Moritz, and T. P. Devereaux, Nat. Rev. Mater. **3**, 312 (2018).
[26] Y. Chen, Y. Wang, C. Jia, B. Moritz, A. M. Shvaika, J. K. Freericks, and T. P. Devereaux, Phys. Rev. B **99**, 104306 (2019).
[27] M. Buzzi, M. Först, R. Mankowsky, and A. Cavalleri, Nat. Rev. Mater. **3**, 299 (2018).
[28] F. Richard, *QED: The Strange Theory of Light and Matter* (Princeton University Press, Princeton, NJ, 1985).
[29] M. S. Tomaš, Phys. Rev. A **51**, 2545 (1995).
[30] J. M. Raimond, M. Brune, and S. Haroche, Rev. Mod. Phys. **73**, 565 (2001).

[31] R. Röhlsberger, K. Schlage, B. Sahoo, S. Couet, and R. Rüffer, Science **328**, 1248 (2010).
[32] R. Röhlsberger, H.-C. Wille, K. Schlage, and B. Sahoo, Nature (London) **482**, 199 (2012).
[33] K. P. Heeg, H.-C. Wille, K. Schlage *et al.*, Phys. Rev. Lett. **111**, 073601 (2013).
[34] K. P. Heeg, C. Ott, D. Schumacher, H.-C. Wille, R. Röhlsberger, T. Pfeifer, and J. Evers, Phys. Rev. Lett. **114**, 207401 (2015).
[35] K. P. Heeg, J. Haber, D. Schumacher *et al.*, Phys. Rev. Lett. **114**, 203601 (2015).
[36] J. Haber, X. Kong, C. Strohm *et al.*, Nat. Photon. **11**, 720 (2017).
[37] J. Haber, J. Gollwitzer, S. Francoual, M. Tolkiehn, J. Strempfer, and R. Röhlsberger, Phys. Rev. Lett. **122**, 123608 (2019).
[38] M. Vassholz and T. Salditt, Sci. Adv. **7**, eabd5677 (2021).
[39] B. W. Adams, C. Buth, S. M. Cavaletto *et al.*, J. Mod. Opt. **60**, 2 (2013).
[40] M. Brown, R. E. Peierls, and E. A. Stern, Phys. Rev. B **15**, 738 (1977).
[41] P. S. P. Wei and F. W. Lytle, Phys. Rev. B **19**, 679 (1979).
[42] R. Röhlsberger, K. Schlage, T. Klein, and O. Leupold, Phys. Rev. Lett. **95**, 097601 (2005).
[43] W. Li, J. Zhu, X. Ma, H. Li, H. Wang, K. J. Sawhney, and Z. Wang, Rev. Sci. Instrum. **83**, 053114 (2012).
[44] X. J. Liu, L. F. Zhu, Z. S. Yuan, W. B. Li, H. D. Cheng, Y. P. Huang, Z. P. Zhong, K. Z. Xu, and J. M. Li, Phys. Rev. Lett. **91**, 193203 (2003).
[45] J. Hill, D. Coburn, Y.-J. Kim, T. Gog, D. Casa, C. Kodituwakku, and H. Sinn, J. Synchrotron Radiat. **14**, 361 (2007).
[46] M. A. MacDonald, S. H. Southworth, J. C. Levin, A. Henins, R. D. Deslattes, T. LeBrun, Y. Azuma, P. L. Cowan, and B. A. Karlin, Phys. Rev. A **51**, 3598 (1995).
[47] P. Eisenberger, P. M. Platzman, and H. Winick, Phys. Rev. Lett. **36**, 623 (1976).
[48] S. Aksela, E. Kukk, H. Aksela, and S. Svensson, Phys. Rev. Lett. **74**, 2917 (1995).
[49] A. F. Van Loo, A. Fedorov, K. Lalumière, B. C. Sanders, A. Blais, and A. Wallraff, Science **342**, 1494 (2013).
[50] X.-C. Huang, Z.-R. Ma, X.-J. Kong, W.-B. Li, and L.-F. Zhu, J. Opt. Soc. Am. B **37**, 745 (2020).
[51] W. Błachucki, J. Szlachetko, J. Hoszowska, J.-C. Dousse, Y. Kayser, M. Nachtegaal, and J. Sá, Phys. Rev. Lett. **112**, 173003 (2014).
[52] K. P. Heeg and J. Evers, Phys. Rev. A **88**, 043828 (2013).
[53] K. P. Heeg and J. Evers, Phys. Rev. A **91**, 063803 (2015).